Comparing Sub-Gap and Above-Gap Pulsed Radiation Sources for Measuring Oxygen Concentration in MgO Using Atom Probe Tomography

Ann N. Chiaramonti[1*], Benjamin W. Caplins[1], Christopher E. Mead[1], Jacob M. Garcia[1,3], and Luis Miaja-Avila[2]

[1] Material Measurement Laboratory, National Institute of Standards and Technology, Boulder, CO USA

[2] Physical Measurement Laboratory, National Institute of Standards and Technology, Boulder CO USA

[3] Present address Applied Materials, Inc., Santa Clara, CA USA

[*] Corresponding Author

Abstract

This paper explores the experimental conditions required to achieve an apparent stoichiometric composition measurement in MgO using near ultraviolet (NUV; 355 nm) and extreme ultraviolet (EUV; ≈29 nm) pulsed laser sources in atom probe tomography. MgO shows strong composition bias under both NUV and EUV laser pulsing. The expected 1:1 bulk composition can be achieved in both EUV and NUV pulsing at high average nanoscale field (low laser pulse energy), as indicated by either the Mg^{++} charge state fraction or the O^{+} ionic fraction in a constant evaporation rate experiment. We report oxygen-rich composition measurements in MgO for the first time. Regardless of the laser wavelength, pulse frequency, or detection rate, the data falls on a single calibration curve of oxygen concentration as a function of the Mg^{++} charge state fraction except at the highest near ultraviolet laser pulse energy tested. These results indicate that for a material with a potential sub-gap absorption mechanism such as MgO, pulsing with higher photon energy does not confer additional benefit in terms of composition measurement. The average nanoscale field is the primary experimental parameter that can be used to achieve a stoichiometric composition measurement, except for when NUV laser pulsing at high laser pulse energy.

Key Words: Atom probe tomography, composition measurement, extreme ultraviolet, insulators.

1. Introduction

Atom probe tomography (APT) is a unique and powerful tool for atomic scale materials analysis. It can provide composition information on arbitrarily shaped nanoscale volumes of material with high analytical sensitivity across the entire periodic table. While precise, it's utility to accurately measure composition in unknown materials or phases can be limited by so-called composition bias. Composition bias is the difference between the true, spatially-resolved composition of the specimen and the apparent spatially-resolved composition as measured by APT, and is often a function of the experimental conditions used to collect the data (e.g. laser pulse energy, ion detection rate, or base temperature) and/or where the particular region of interest (ROI) is placed. For example, it has been shown that a variety of compound and wide bandgap semiconductor materials exhibit varying apparent composition as a function of the experimental conditions [1–17]. Strong compositional bias was demonstrated on a variety of iron oxides [18–22], and a large study of mineralogical materials demonstrated that some species such as arsenopyrite (AsFeS) and barite ($BaSO_4$) can exhibit strong compositional [23].

For materials such as pure single crystal GaN, that can only exist in the stoichiometric state, this error from compositional bias can be overcome by performing careful calibration experiments or by applying known tooling factors to the measurement results. However, if the material or phase of interest is unknown a priori (e.g. identifying the phase of a mixed cation transition metal corrosion product) or if the system can exist as several distinct, closely related compounds (e.g. the series of chromium or uranium oxides) or accommodate some level of non-stoichiometry on a continuum (e.g. through oxygen

vacancy in tungsten oxides or iron vacancies in iron sulfides), then performing atom probe tomography to determine the actual composition of an unknown specimen is nearly impossible.

Oxides comprise a large class of technologically important materials that are difficult to measure accurately in atom probe tomography due to several inter-related factors, many of which are not fully understood at this time. They often show strong composition bias, and the general trend is that while occasionally there are reports of stoichiometric or oxygen-rich measurements [24–26], oxides are almost always measured to be oxygen deficient in atom probe tomography [8,18–22,27–45]. Recently, it was shown that using coherent extreme ultraviolet (EUV) radiation to perform atom probe tomography may confer some benefit in terms of composition bias and measuring the oxygen concentration in amorphous SiO_2, perhaps due to an absorption-localized heating mechanism or possibly even athermal ionization [26].

Building on those results, MgO is an interesting test case material to examine using EUV radiation for several reasons. The bulk optical bandgap of MgO is 7.8 eV yet MgO has been routinely analyzed in APT using near ultraviolet (NUV; λ = 355 nm, E_{photon}= 3.5 eV) and even green (λ = 532 nm, E_{photon}=2.3 eV) lasers [1,46–52]. However, there are no reports in the literature of a stoichiometric MgO composition measurement in APT where the peak at 16 m/z was ranged as O^+ instead of O_2^{++}. Labeling the 16 m/z peak as O_2^{++} increases the apparent oxygen concentration, however ^{18}O labeled studies have shown that the 16 m/z peak consists of only O^+ in other oxides [22,28]. Pump-probe laser desorption studies on cleaved single crystal surfaces using deep ultraviolet (E_{photon} = 4.7 eV and 6.4 eV) excitation have shown that both neutral ion and positive ion emission occurs in MgO [53–56]. It has been posited that absorption and ionization of MgO under sub-gap, near ultraviolet (NUV) radiation in APT proceeds through a process involving photoexcited holes [46,57,58]. Further, these holes may contribute to the creation of oxygen neutrals that desorb as atomic O or molecular O_2, thus greatly affecting composition

measurements [59]. Other studies point out the possible contribution to absorption of Franz-Keldysh effects, defects introduced during sample preparation, and importantly, closing of the bandgap at the surface due to the high standing voltage [60–62]. An open question is whether performing atom probe tomography using EUV radiation, which is well above the bulk optical bandgap of MgO, would produce the same results, occur by the same mechanism(s), and whether EUV radiation would reduce composition bias in the measurement of oxygen concentration compared to NUV laser pulsing.

The goal of this work is to study the field evaporation behavior of MgO<001> under EUV laser illumination and compare that to results obtained using an NUV laser source. The laser pulse energy and detection rate were varied for both wavelengths. The pulse frequency (repetition rate) was varied for the NUV study; the EUV APT operates at a fixed pulse frequency. We compare the observed composition bias and attempt to understand the conditions that lead to a stoichiometric measurement in this material.

2. Experimental Methods

Single crystal, single-side polished MgO<001> substrates used for this study were purchased from MTI Corporation[1]. APT specimens were prepared using standard lift-out procedures [63]. Wedges were mounted on Hitachi NanoMesh Si-based half-grids and shaped using 30 kV $^{69}Ga^{+}$ ions with a final polish at 5 kV. The resulting tips had shank half-angles in the range of approximately 7° to 10°. Atom probe tomography was performed on two straight flight path local electrode atom probe instruments. The first was a CAMECA LEAP 4000X-Si near-ultraviolet (NUV) commercial instrument with a wavelength of λ=355 nm (E_{photon}=3.5 eV). The second was the National Institute of Standards and Technology (NIST) Extreme

[1] Commercial equipment, instruments, or materials are identified only in order to adequately specify certain procedures. In no case does such identification imply recommendation or endorsement by the National Institute of Standards and Technology, nor does it imply that the products identified are necessarily the best available for the purpose.

Ultraviolet Atom Probe (EUV APT), which is based on a LEAP 4000X-Si platform and used a wavelength of approximately $\lambda \approx 29$ nm ($E_{photon} \approx 41.85$ eV). For more information on the details of the EUV atom probe instrument and generation of coherent EUV light for atom probe tomography, please see Refs. [64,65]. APT data were collected in constant detection rate (DR) mode with a constant laser pulse energy for each experimental condition. A variety of laser pulse energies were tested with a base temperature setpoint of 50 K and DRs of 1 % and 10 % (0.01 ions/pulse and 0.1 ions/pulse, respectively). The pulse frequency of the EUV APT was 25 kHz. NUV data was collected at both 25 kHz and 250 kHz pulse frequencies. Approximately 500,000 total ions were collected at each experimental condition.

The laser pulse energies in this study were varied by orders of magnitude in both systems, as much as the instrument would practically allow. In the NUV system five orders of magnitude could be achieved whereas in the EUV system, four orders were achieved. The data were collected using five different specimens and laser pulse energies were varied randomly for cases where the same nominal pulse rate and detection rate were used for sequential experiments. The laser pulse energies were varied randomly in order to decouple the decrease in field accompanying any (slight) increase in radius as the specimen is evaporated.

In the EUV system, laser pulse energy orders of magnitude are reported as “percent transmission” (% T). This is because the laser pulse energy used for an experiment is controlled by inserting combinations of thin (200 nm – 2,000 nm) Al filters into the beamline [64]. These are indexed by the measured fractional transmission of the various filter combinations (compared to having no insertable filters; there is always one fixed filter that is not varied) onto a photodiode and recorded as “% T”. Since the actual EUV experiments were performed by physically inserting combinations of Al filters to vary the fractional transmission by orders of magnitude, the EUV data will be presented as % T.

This % T can be converted into a nominal laser pulse energy in joules using the known responsivity curve of the photodiode. However, this number is not directly useful for comparison with NUV data since the focused laser spot size and therefore the fluence and number of photons per unit area in these systems are very different. For reference, assuming a FWHM beam diameter of ≈2 um in the NUV and ≈12 μm in the EUV, 5 % T in the EUV system is approximately equivalent to 5 pJ of laser pulse energy (but spread over a much larger spot). In terms of equivalent fluence, which accounts for the spot size, 0.1 pJ in the commercial LEAP 4000/NUV system (approx. $6x10^{-6}$ J/cm^2) is approximately the same fluence as 5 % T in the EUV system ($3x10^{-6}$ J/cm^2).

Data were analyzed using CAMECA IVAS 3.8 commercial atom probe software. The peak at 16 m/z was ranged exclusively as O^+ based on previous reports which used ^{18}O to verify that the peak at 16 m/z did not contain O_2^{++} for other oxides [22,28]. Ranging the 16 m/z peak as O_2^{++} as was done in [49] would result in an artificially high apparent oxygen concentration.

Mass calibration was performed using only the single-hit counts for the Mg^+ peak at 24 m/z. In both the NUV and EUV datasets, the Mg^+ peaks showed peak splitting, the nature and magnitude of which varied as a function of the laser wavelength and laser pulse energy (see below). For the purposes of mass calibration, it was assumed that the peak with the highest number of single hit counts would be placed at the proper location for the expected $^{24}Mg^+$ isotope. For the NUV data, this method ensured that there was always $^{24}Mg^+$ peak present for every laser pulse energy but resulted in consistent pre-peaks in the data. Conversely, the EUV data calibrated the same way shows post-peaks or bimodal tails for the $^{24}Mg^+$ peaks.

The Decomposition of Peaks algorithm within IVAS 3.8 was used for all data sets to separate the contributions of the O_2^+ ion and the Mg_2O^{++} ion in the peaks near 32 m/z. This method employs a local range assist power law-based background subtraction method that also includes a global time of flight correction. We note that alternative background subtraction methods (e.g. local range assisted with constant background, or only the global time-of-flight correction) may yield different results (see Supplementary Information). The default ranging scheme in the Decomposition of Peaks algorithm (0.1 m/z before, 0.2 m/z after the peak for a total constant range of 0.3 m/z) was used for all peaks except for the Mg^+ ions. For the Mg^+ peaks, the presence of consistent pre-peaks in the NUV data and the large, bimodal tails in the EUV data necessitated the ranging of these ions manually. A similar approach was used to the default method, where the ranges were set at 0.1 m/z before the first peak and 0.2 m/z after last peak. Note that this method may result in a total range for Mg^+ ions that is often larger than 0.3 m/z. These ranging schemes (16 m/z = O^+ and Mg^+ ranged manually) may skew the results slightly toward Mg-rich concentrations on the order of ~ 0.1 % for the highest laser pulse energies as the total counts in the Mg^+ peaks are very low, especially in the NUV data. Despite the alternate ranging methods used, the overall trend in MgO composition as a function of LPE reported below remains consistent.

The Mg^{++} charge state fraction (CSF) is defined as $^{24}Mg^{++}/(^{24}Mg^+ + ^{24}Mg^{++})$, as the $^{24}Mg^{+++}$ ion was not observed in our data. Only ^{24}Mg ions were used as they avoid any possible contribution of hydrides to the calculation. The CSF was calculated using the entire ROI. Thus, it represents a spatial average (x-y, and z) and neglects variation with depth as well as any localized perturbations that come from the indications of crystallography (crystal pole, zone lines) in the desorption map, when present [66]. For some experimental conditions, there may be variations of the ionic charge states due to the strong <001> pole and associated zone lines, as seen in other crystalline materials [67]. However, since all tips were fabricated from a single crystal and are the same crystallographic orientation, any zone- or

crystallography-related artifacts are radially symmetric and would contribute the same to all data. We assume that the CSF is positively correlated with the nanoscale field [68] (e.g. these materials qualitatively obey the theory of post-field ionization [69]), and so we refer to the nanoscale field specifically as the “average nanoscale field” to emphasize that it is a spatial average.

The CSF was used rather than the charge state ratio (CSR; defined as Mg^{++}/Mg^{+}) as it does not suffer from the divide by zero issue that arises for high CSRs. Using the CSR instead of the CSF lead to large variation in the calculated CSF or even an undefined number depending on exactly how the peaks were ranged and how the background was subtracted.

Due to the various factors involved in creation of the EUV light and the nature of high harmonic generation in a gas-filled capillary (e.g. the harmonic character of the spectrum can vary day to day [70], as well as factors related to long-term pump laser diode stability, steering and focusing the beam, and the photodiode response, we estimate the error associated with the reported EUV laser pulse energy (% T) is roughly between 20 % to 30 %. This is based on our characterization and tracking over time. This does not affect the main results and interpretation presented here as the results are presented on a log scale with four orders of magnitude variation in laser pulse energy.

Statistical (Type A) uncertainty for the composition and CSF calculations is on the order of a tenth of a percent or less and does not affect the results or the conclusions presented from the data. We believe a more significant contribution to the uncertainty in the measurement is the various sources of error that contribute to Type B uncertainty [71,72]. Type B uncertainty is the component of the overall uncertainty arising from systematic effects. These components of uncertainty are not unique to insulators and apply to all atom probe tomography measurements. These include for example the method of peak ranging

(e.g. was the full-width tenth-maximum, full-width half-maximum, or a fixed range used), the method of background subtraction (e.g. was the global time of flight or a local-range assist method in m/z space used), and any additional error associated with using isotopic abundances as the basis for the Deconvolution of Peaks algorithm within CAMECA IVAS [73,74]. We estimate Type B uncertainty to be on the order of +/- 1 %.

3. Results

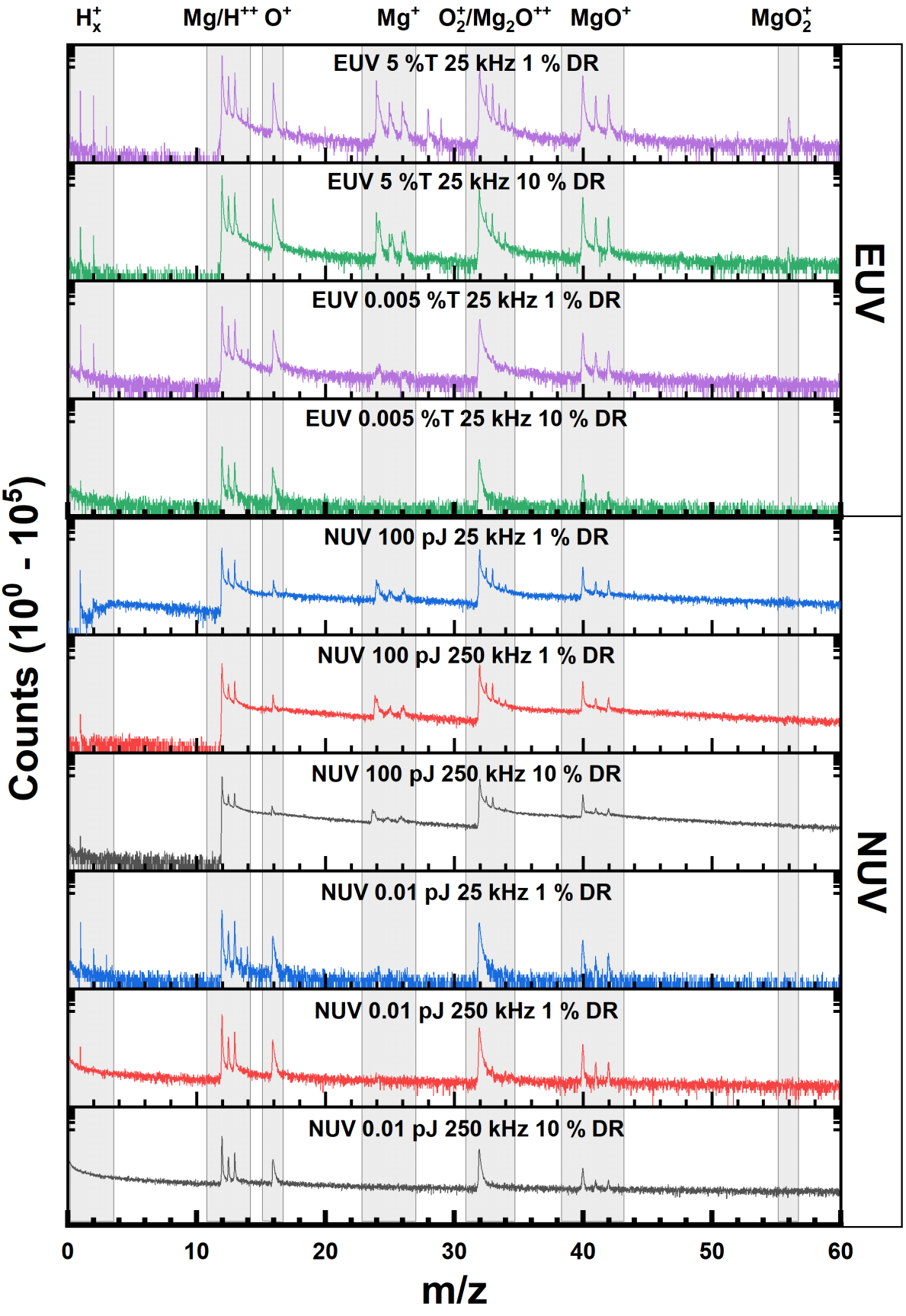
H_x^+
Mg/H^{++} O^+
Mg^+
O_2^+/Mg_2O^{++}
MgO^+
MgO_2^+
EUV 5 %T 25 kHz 1 % DR
EUV 5 %T 25 kHz 10 % DR
EUV 0.005 %T 25 kHz 1 % DR
EUV 0.005 %T 25 kHz 10 % DR
NUV 100 pJ 25 kHz 1 % DR
NUV 100 pJ 250 kHz 1 % DR
NUV 100 pJ 250 kHz 10 % DR
NUV 0.01 pJ 25 kHz 1 % DR
NUV 0.01 pJ 250 kHz 1 % DR
NUV 0.01 pJ 250 kHz 10 % DR
EUV
NUV
Counts (10^0 - 10^5)
0
10
20
30
40
50
60
m/z

Figure 1: Raw mass spectra (not background corrected) binned at 0.01 m/z per bin and displayed on a logarithmic scale ranging from 10^0 to 10^5 counts. Shown here are the highest and lowest laser pulse energies examined for both NUV and EUV covering the range of pulse frequencies (25 kHz, 250 kHz) and detection rates (1 % and 10 %) studied. The mass spectrum ion assignments are denoted along the top. Note: the regions in gray are not the ranges used for compositional analysis; they are simply shown to guide the eye as to the assigned ion type for each set of peaks. For H_x^+, $1 \leq x \leq 3$. This data is available at https://data.nist.gov/od/id/mds2-4005.

Figure 1 shows representative mass spectra covering the range of experimental conditions tested here. For space and clarity, only the mass spectra for the highest and lowest laser pulse energy for each wavelength and each condition (pulse frequency and detection rate for NUV and detection rate for EUV) are shown. The regions shaded in gray were not used for the calculation of composition; instead, they are shown to guide the eye as to the assigned ion type for each set of peaks. The mass spectra are comprised of the following peaks, which are not always present under all conditions: H^+, H_2^+, H_3^+, Mg^{++}, MgH^{++}, O^+, Mg^+, Mg_2O^{++}, O_2^+, MgO^+, MgO_2^+, and Ga^+. The Ga concentration for the datasets ranged from undetected to 0.39 at. %. Of the 23 datasets used in this paper, 20 had Ga concentrations less than 0.1 at. %. Multiple hit events for these samples range from 27 % to 73 %. Multiple hit percentages are higher for the EUV data compared to the NUV data. Also, in general, multiple hit events are higher for lower laser pulse energies and higher detection rates. As expected, they are related to the average nanoscale field. A table containing the measured Ga concentration and the multiple hit percentage can be found in the Supplementary Information. There are what appear to be very small (< 10 counts) Si-related peaks in the mass spectrum for some of the datasets. These likely come from parasitic spires on the Si NanoMesh grid. These were not included in the calculation of oxygen concentration.

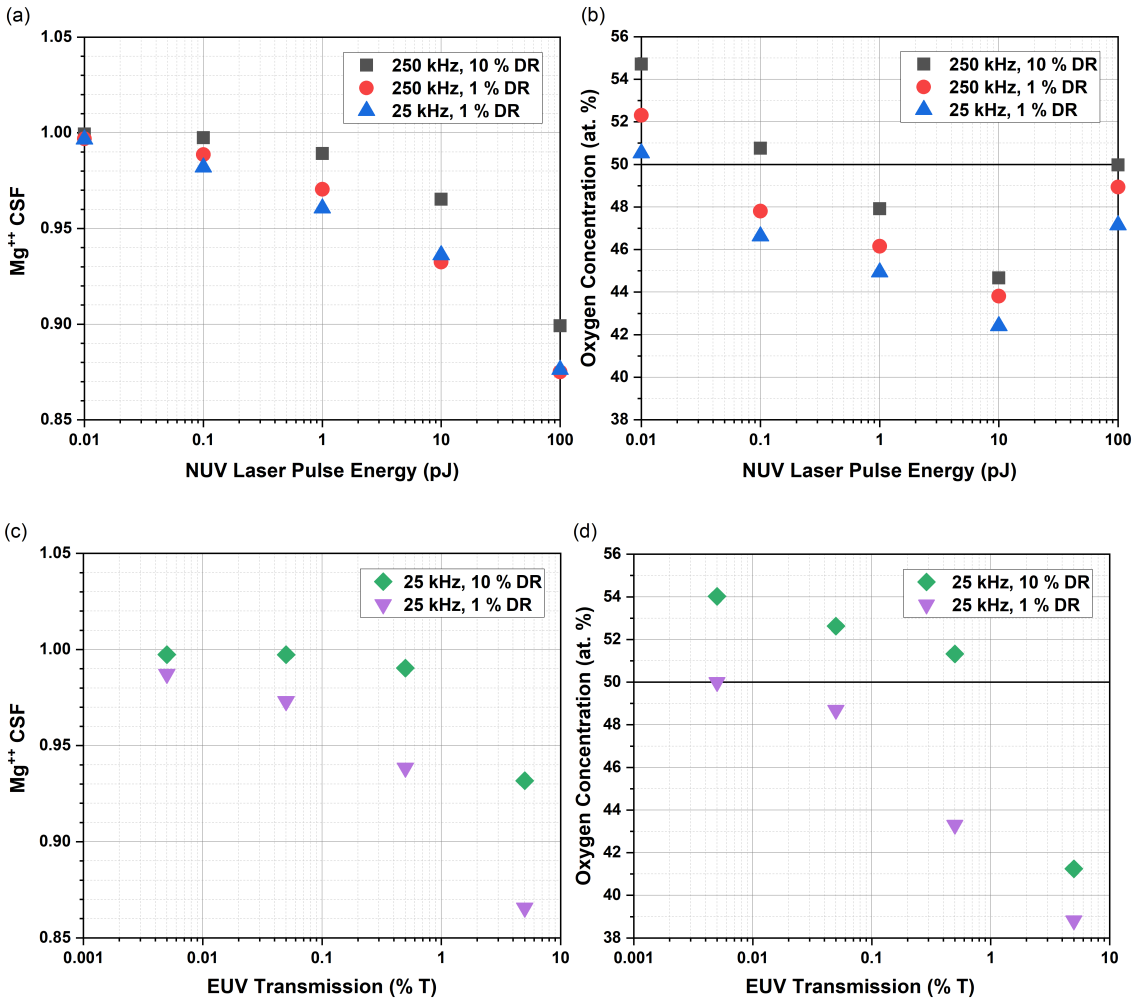

Figure 2: (a) Mg^{++} charge state fraction as a function of NUV laser pulse energy. (b) Measured oxygen concentration as a function of NUV laser pulse energy. (c) Mg^{++} charge state fraction as a function of EUV % transmission. (d) Measured oxygen concentration as a function of EUV % transmission. For both data sets, the average Mg^{++} charge state fraction is monotonic and non-linear with the laser pulse energy (or % T). In (b,d) the expected stoichiometry is indicated.

The Mg^{++} CSF and the apparent oxygen concentration as a function of laser pulse energy or % T are reported for both NUV and EUV wavelengths in Figure 2. For both data sets, the average Mg^{++} CSF is monotonic and non-linear with the laser pulse energy with the Mg^{++} CSF increasing as the laser pulse energy is decreased. This makes intuitive sense in a constant detection rate *laser pulse* experiment if one

assumes that the CSF is correlated with the average nanoscale field, as proposed by Kingham [69]. Any potential increases in radius that occur as a specimen is field evaporated will increase the field of view thus decreasing both the overall flux per unit area of the tip and the average nanoscale field over time. However, these overall field decreases are far outweighed by the surface field changes necessary to maintain a constant evaporation rate because of the order of magnitude changes in laser pulse energy and therefore evaporation temperature [4,75].

For a given laser pulse energy, the Mg^{++} CSF increases as the detection rate is increased from 1 % to 10 % as the specimen necessarily experiences a higher average surface electric field at a higher detection rate. This suggests, again, that the Mg^{++} CSF is well correlated with the average surface electric field in these experiments. Finally, for NUV laser pulsing, the laser pulse frequency does not appear to have a clear, strong effect on the observed Mg^{++} CSF.

The apparent oxygen concentration measured here varies as a function of laser pulse energy for both EUV and NUV experiments. In general, except for the NUV data collected at 100 pJ (regardless of the pulse frequency or the detection rate), the oxygen concentration increases with decreasing laser pulse energy and increasing Mg^{++} CSF (average nanoscale field). This observation is consistent with other reports in the literature that measured the oxygen concentration as a function of the laser pulse energy [49] or the Mg^{++} CSR [1]. However, unlike in those studies, we report measured oxygen concentrations that reach the expected 50 % value and, in some cases of high average nanoscale field, exceed that value while ranging the peak at 16 m/z as O^+ as suggested by previous ^{18}O isotope labeling studies in other oxides [22,28].

4. Discussion

For both the NUV and EUV data, the peak splitting of the Mg^+ ions in this study presented a unique challenge for mass spectrum calibration and ranging. In all the NUV data collected (Figure 3), the Mg^+ ions showed peak splitting where the magnitude of the relative sizes of the split peaks varied proportionally with the laser pulse energy. For consistency, the $^{24}Mg^+$ peak with the highest single hit count was used for mass calibration of the Mg^+ ions. For the NUV data, this highest single count peak was always also the higher m/z peak of the two. The result is that the NUV data consistently shows Mg^+ pre-peaks throughout the five orders of magnitude range of laser pulse energies studied here. Since the relative height of the lower m/z peak increases as the laser pulse energy is increased, this scheme leads to the consistent presence of a $^{24}Mg^+$ peak in all the NUV data. If the lower m/z peak had been used as $^{24}Mg^+$ to calibrate the data, then the prominent sharp "tail", offset by ~ +0.1 m/z, would eventually overtake the height of the actual peak at 24 m/z. Notably, all of the other peaks present in the mass spectrum showed a sharp onset, did not show signs peak splitting, and did not present a challenge for mass spectrum calibration nor ranging.

In ranging this NUV data with such prominent peak splitting present, the Mg concentration would be slightly underestimated when using the default 0.3 m/z range in the IVAS Decomposition of Peaks tool for several reasons. First, when using the default range scheme, the automatic "local range assist" background subtraction method for this peak is not accurate as it considers the pre-peak as a part of the local background when performing the calculation and setting the local background level. This underestimates the amount of Mg^+ as a result. Second, in using the default ranges, the significant pre-peak would nearly always be excluded, even though in some cases the counts are nearly equal to or higher than the counts in the higher m/z peak. In short, the default ranging scheme ignores the pre-

peak, causes errors in the background subtraction algorithm, and thus artificially undercounts the Mg concentration.

Ranging the Mg^+ peaks manually as previously described ensures that Mg is not systematically undercounted and also ensures that the background subtraction is accurate and the oxygen-rich Mg concentrations measured in this study are reasonable. The Mg^{++} peak is always the highest peak in the overall mass spectrum. In any case, the counts in the Mg^+ peak are relatively low even for high laser pulse energies/small CSFs, and so changing the ranging of the Mg^+ ions does not change the overall measured composition notably. If the Mg^+ peaks were ranged using the default method, the measured composition was found to vary by less than 0.1 % for the highest laser pulse energies.

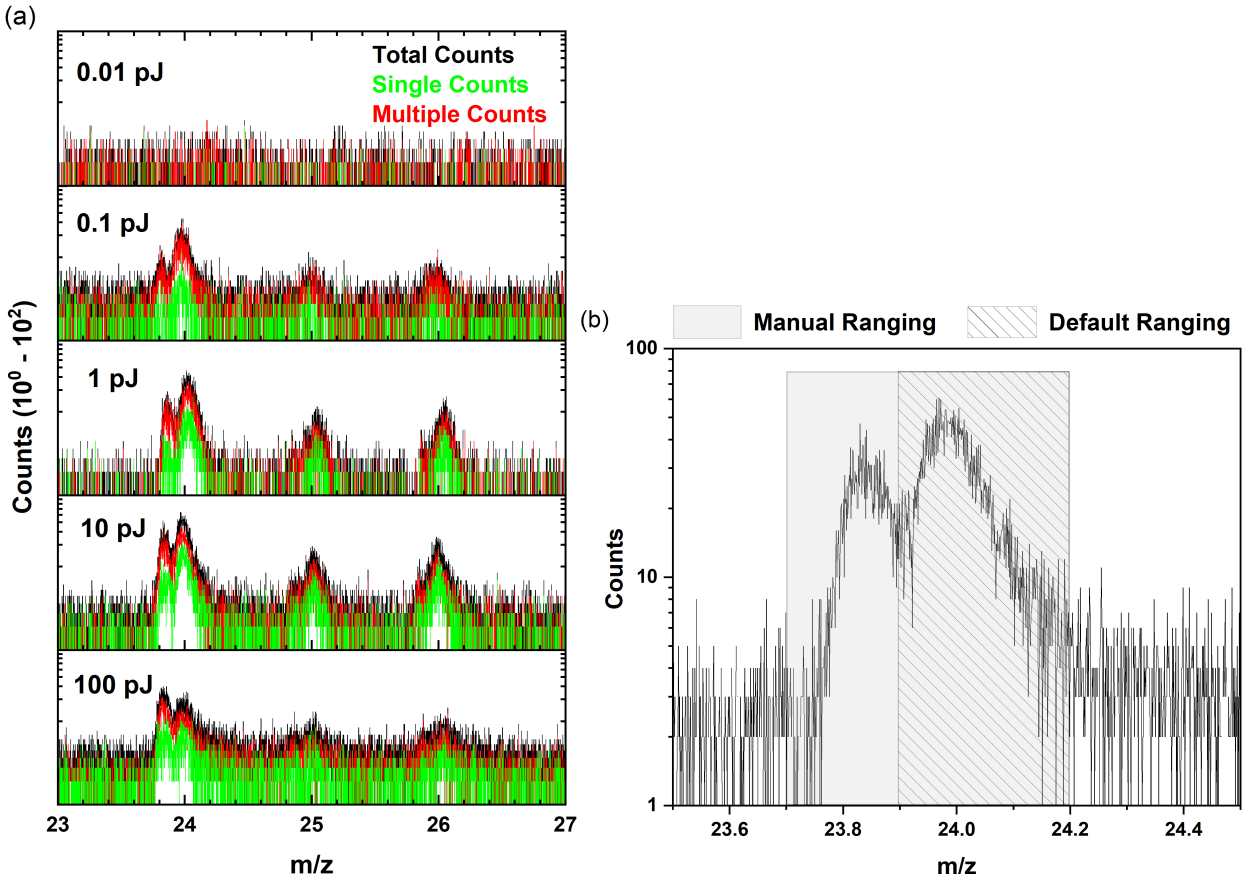

Figure 3: (a) Unbinned, uncorrected 250 kHz NUV mass spectra near 24 m/z (Mg^+) showing total counts, single hit counts, and multiple hit counts. In the NUV data, the relative height of the apparent pre-peak

292 increases with increasing laser pulse energy and at 100 pJ the peak heights are nearly identical. (b) Mass
293 spectrum near 24 m/z for the 10 pJ dataset showing the result of the default Decomposition of Peaks
294 ranging scheme (-0.1 m/z, + 0.2 m/z) compared to the manual ranging scheme described above. The
295 default ranging scheme ignores the pre-peak, causes errors in the background subtraction algorithm, and
296 thus artificially undercounts the Mg concentration.
297
298 The EUV data for the Mg^+ ions (Figure 4) also showed complex behavior as a function of laser pulse
299 energy. Mass calibration was performed similarly to the NUV data, e.g. the peak with the highest single
300 hit counts (in contrast to the NUV data, for EUV is always the lower m/z peak) was used for the $^{24}Mg^+$ ion
301 in mass calibration. For EUV ranging, again, using the default 0.3 m/z range in the Decomposition of
302 Peaks code in IVAS would result in undercounting the Mg due to the large, prominent bimodal tail. These
303 peaks were also ranged manually in the same way as the NUV, often resulting in ranges > 0.3 m/z. We
304 believe that this method more accurately represents the Mg counts measured in these experiments.

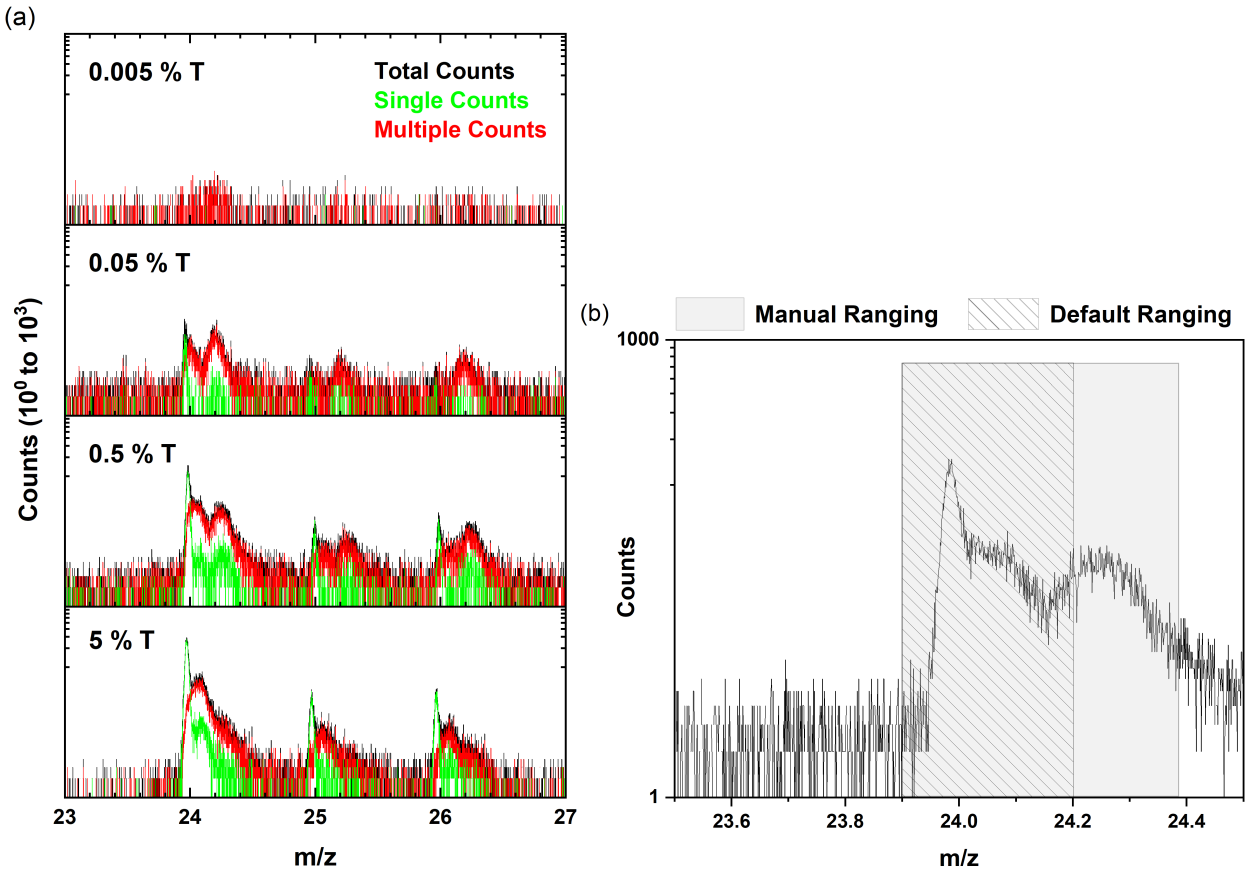

Figure 4: (a) Unbinned, uncorrected EUV mass spectra near 24 m/z (Mg^+) showing total counts, single hit counts, and multiple hit counts. In the EUV data, the relative height of the post-peak increases with decreasing laser pulse energy and at 0.05 % T the peak heights are nearly identical. (b) Mass spectrum near 24 m/z for the 0.5 % T dataset showing the result of the default Decomposition of Peaks ranging scheme (-0.1 m/z, + 0.2 m/z) compared to the manual ranging scheme described above. The default ranging scheme ignores the significant post peak(s).

One possible source of peak splitting in APT mass spectra is an incomplete voltage and bowl correction. However, when this occurs, it applies to all peaks similarly. Since there are also peaks in the mass spectra that have a sharp onset and do not show splitting (e.g. O^+, O_2^+/Mg_2O^{++}, MgO^+, etc.), we do not believe this observation is a result of a bad voltage/bowl correction. Another possible source of peak splitting is

an electrostatically induced systematic energy deficit [76]. Such deficits have been observed previously in insulating materials; however, a correction was applied to the data here and it did not improve the mass spectra. The peak splitting observed here also does not appear to be the results of a fast versus slow cooling effect (so-called “bright side/darks side” effect) as had been observed in previous studies of MgO and other oxides using green and NUV light [48,77]. This was verified as seen in Figure 5 by spatially sub-ranging the detector relative to the direction of the incident laser illumination and observing the relative position of the Mg^+ peaks. For the laser fluences used here, there was no observed shift in the position of the Mg^+ peaks in the mass spectrum as a function of the position on the detector.

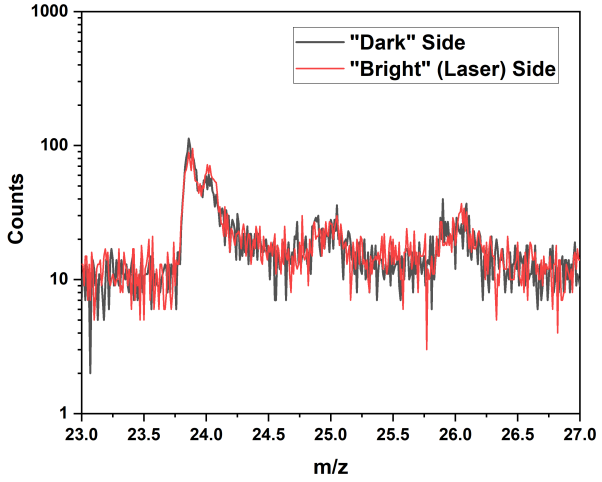

Figure 5: Uncorrected Mg^+ mass spectra for 100 pJ 250 kHz NUV data collected at 1 % DR and binned to 0.01 m/z per bin. The detector was spatially segmented as described in [77] and the resulting mass spectra are plotted above. There is no shift in the Mg^+ peaks as a result of the spatial position on the detector, implying that the peak splitting is not the result of slow cooling as had been observed previously using a different type of instrument with a much larger (100 μm) focused spot and 343 nm light [48].

Instead, we suppose the observed Mg^+ peak splitting may be attributed to complex ion dissociations e.g. $Mg_2O^{++} \rightarrow Mg^+ + MgO^+$, $MgO^{++} \rightarrow Mg^+ + O^+$, or $MgO_2^+ \rightarrow Mg^+ + O_2$. Such dissociations are frequently observed in APT of various materials including oxides, carbides, and nitrides [2,78–82] . In NUV pulsing the Mg^+ pre-peaks (containing a high proportion of multiple hit counts) could be explained by the dissociation $MgO^{++} \rightarrow Mg^+ + O^+$. Since Mg^+ is the higher m/z daughter product of the dissociation, it would appear at slightly lower m/z than expected (e.g. as a pre-peak) compared to if had it ionized and desorbed directly [76,83]. Conversely, for EUV pulsing the dissociation of $Mg_2O^{++} \rightarrow Mg^+ + MgO^+$ leads to the lighter daughter ion (Mg^+) appearing at a higher m/z than expected (e.g. as a tail). This peak splitting is a function of the laser wavelength only in as much as the laser wavelength and the associated details of the evaporation process may lead to the formation and dissociation of different species of complex ions. Of note, we have also collected data from the same MgO single crystal in a CAMECA Invizo 6000 straight flight path atom probe instrument equipped with a deep ultraviolet laser (λ=257 nm; E_{photon}=4.8 eV). That data was collected at similar conditions (e.g. 1 pJ, 50 kHz, and 1 % DR) and we observed splitting of the Mg^+ peaks (see Supplementary Information). Collecting data from the same specimen on three different straight flight path atom probe instruments all with relatively small spot sizes (≈ 2 μm – 3 μm for the commercial instruments and ≈12 μm for the EUV instrument) demonstrate that it is not an instrument issue.

The idea that the Mg^+ peaks are split due to dissociation-related energy deficits is supported by some *ab initio* calculations as well as density functional theory calculations on MgO clusters that show that Mg should primarily evaporate directly into the Mg^{++} charge state [57,58,61,84]. This supports the idea that Mg^+ detected in the mass spectra observed here may come at least partially from complex ion dissociation. There are faint dissociation tracks in correlation histograms (see Supplementary Information) for both data sets corresponding to these dissociation pathways, but due to the relatively

low number of total counts in each mass spectrum, there was no further attempt at quantification. The lack of clear dissociation tracks does not negate the possibility that complex ion dissociations contribute to the peak splitting observed here. Complex or ultrafast dissociations (e.g. a 3-body dissociation or homolytic dissociation) can be difficult to detect and interpret in a correlation histogram even without sparse data. Note that peak splitting of this nature would not be observed in an instrument equipped with a reflectron energy compensating lens, and this may explain why such peak splitting was not noted in previous studies of single crystal MgO [49,50].

As seen in Figure 3 for the NUV data, the multiple hit count for the Mg^+ peaks were always higher than the single hit counts for every laser pulse energy tested. In contrast, Figure 4 demonstrates that for the EUV data the single hit count was large for high % T (high "laser pulse energy", corresponding to lower average nanoscale fields) and decreased relative to the number of multiple counts as the % T decreased. At the lowest % T (highest average nanoscale field), the total Mg^+ counts were very low and there were virtually no single hits.

A calibration curve (Figure 6) can be created for MgO by combining the data in Figure 2. All the data, independent of the laser wavelength, pulse frequency, and detection rate, follows a curve - *except for the 100 pJ NUV experiments* - and can prescriptively provide the Mg^{++} CSF required to achieve a stoichiometric measurement in this material. This points to the importance of the apex electrostatics and the importance of the average surface electric field in determining the oxygen stoichiometry in this strongly insulating, ionic material, at least at moderate laser pulse energies (defined here as 10 pJ and below, for NUV pulsing).

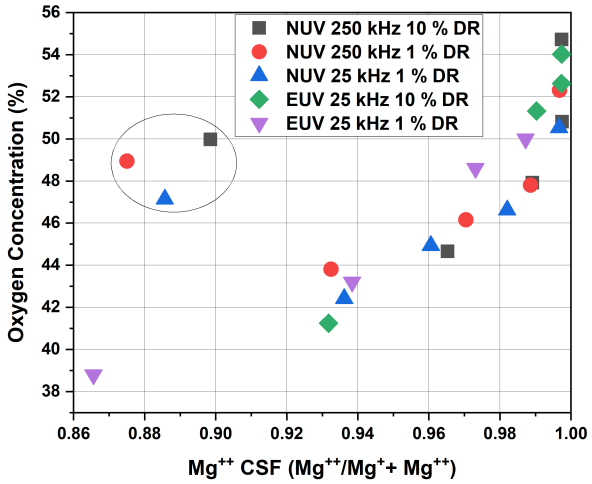

382

383 Figure 6: Oxygen concentration as a function of the Mg^{++} CSF (a proxy for the average nanoscale field).

384 The horizontal line at 50 at. % indicates the expected stoichiometric oxygen concentration. Except for the

385 100 pJ NUV data (circled), the rest of the data forms a "calibration curve" and demonstrates that higher

386 Mg^{++} CSFs yield higher measured oxygen concentrations. This curve also demonstrates that regardless of

387 the laser wavelength, oxygen concentrations of greater than 50 % can be observed at high average

388 nanoscale fields as the Mg^{++} CSF approaches 1.0.

389

390 In attempt to further understand the unexpectedly low oxygen concentration measured at 100 pJ (given

391 that the Mg^{++} CSF curve in Fig. 2a is monotonic and decreasing as expected for a constant evaporation

392 rate experiment), the O^+ ionic fraction (IF) defined as $O^+/(O^+ + O_2^+)$ was calculated. This serves as a

393 second, independent indicator of the relative magnitude of the nanoscale surface field. In fact, in some

394 transition metal oxides, O/O_2 ratios have been shown to be a better, more reliable indicator of the

395 surface electric field conditions compared to metal cation ratios [19–21]. However, as shown in Figure 7

396 the O^+ IF also shows a strong correlation with laser pulse energy that is nearly linear on a semi-log plot.

397 This indicates that the nanoscale surface field present at 100 pJ trends as expected. At 100 pJ, MgO

398 appears to have an artificially "high" apparent measured oxygen concentration given the observed Mg^{++}

399 CSF. It is the measured oxygen concentration that is the anomaly, not the average nanoscale field. This

was consistent and repeatable in our experiments. To further verify the data collected at 100 pJ is not a discontinuous outlier, additional measurements were made for NUV pulsing at 250 kHz and 1 % DR at 25 pJ, 50 pJ, and 75 pJ (see Supplementary Information). The curve of laser pulse energy versus oxygen concentration for NUV pulsing is continuous, thus demonstrating that the 100 pJ data is real and not an outlier or an issue with the laser (e.g. a bad spot on the neutral density filter). Finally, 2D detector maps of the Mg^{+} and Mg^{++} ion concentrations (see Supplementary Information) verify that the specimens show the same crystal pole in the same location as well as display radial symmetry even at the highest NUV laser pulse energies. This means that the spatial average CSF calculated using the entire ROI is a valid assumption, even at 100 pJ.

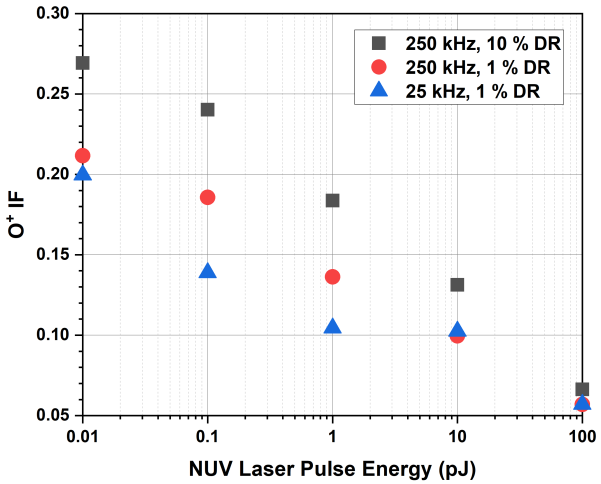

Figure 7: O^{+} ionic fraction, defined as $O^{+}/(O^{+} + O_2^{+})$, as a function of NUV laser pulse energy.

Since this anomaly is only observed at the highest NUV laser pulse energies tested here, it may be attributed to non-linear absorption or strong multiphoton effects. High NUV laser pulse energies may also influence the formation and desorption of certain ion species compared to other ions. For example, at the highest EUV laser pulse energies, we observe the formation of the MgO_2^{+} ion. This ion may dissociate to $Mg^{+} + O_2$, leading to a loss of oxygen through neutral formation. This ion, and therefore potential channel for loss of oxygen, is not observed in the NUV data since this ion is not formed. Thus,

418 at high NUV laser pulse energies more ionic oxygen may be detected. The high NUV laser pulse energy
419 may also lead to scenarios where co-evaporation, multiple hits, and/or significant detector deadtime
420 lead to the undercounting of Mg species, as has been described previously for other materials [2,73].
421
422 This high laser pulse energy effect – apparently unrelated to the average surface electric field - has not
423 been previously reported in the two other studies of MgO that measured the composition as a function
424 of the laser pulse energy or CSR using NUV laser pulse instruments. This is expected for the LaWaTAP
425 instrument [1] as the maximum fluence achievable on that tool is orders of magnitude less than that of
426 the commercial NUV LEAP operating at 100 pJ. The other study with 100 pJ NUV laser pulsing [49] used a
427 LEAP 4000X-HR equipped with an energy-compensating reflectron lens. Reflectron-equipped LEAP
428 instruments have an entirely different electrostatic flight path compared to straight flight path
429 instruments (field free flight path versus a biased drift tube with a negative bias on the multi-channel
430 plate detector) as well as a different field of view [79]. The detection of dissociation events and peak
431 splitting would all be different in these two instruments. If ions dissociate differently in the field-free
432 flight path versus the biased flight path, and/or certain dissociation products are not detected, this can
433 lead to differences in the measured oxygen concentration. Other possibilities are subtle differences in
434 the specimens themselves such as the extent of Ga^{+} implantation and or lattice damage, impurities,
435 specimen shape, or possibly also differences in the electrostatics that come from using a microtip
436 coupon array versus a TEM half-grid with a very high aspect ratio.
437
438 5. Summary and Conclusions
439 MgO qualitatively obeys the Kingham theory of post-field ionization in that higher average nanoscale
440 fields yield higher Mg^{++} CSFs. This material exhibits strong compositional bias under both EUV and NUV
441 laser pulsing. We have demonstrated that it is possible to achieve stoichiometric and even oxygen-rich

measurements of MgO under condition of high average nanoscale fields without ranging the peak at 16 m/z as O_2^{++} and irrespective of laser wavelength. Anion-rich measurements have been shown previously in other materials (e.g. GaN, AlN, CdTe)[1–3,6,7], but as far as we are aware, none have been reported in MgO. To optimize (achieve a stoichiometric measurement) laser-pulsed APT measurements in MgO, either a NUV or EUV laser can be used provided the experimental conditions allow for a relatively high average nanoscale field (e.g. Mg^{++} CSFs approaching 1.0). In any case, due to the possibility of oxygen-rich experimental conditions at very high average nanoscale fields, calibration curves should always be created to quantify the compositional bias under the details of the exact experimental conditions employed (e.g. laser wavelength, tip shape, specimen carrier mount, instrument electrostatics, base temperature, vacuum conditions, etc.). Using high laser pulse energies in the NUV should be avoided due to the non-monotonic nature of the NUV material response.

The laser-assisted field evaporation of MgO is a complex process involving many competing factors, and the experimental mass spectra shown here are proof of that. The dominant factor in determining the measured composition of this material by APT is the average nanoscale field as evidenced by the fact that the CSF vs oxygen concentration data fall along a single curve (except for 100 pJ NUV) for the experimental parameters (including EUV and NUV) explored here. Higher average surface electric fields generally lead to higher apparent measured oxygen concentrations. However, our results show that there are other complex factors at play and care must be taken especially when experiments are performed at high laser fluence. The NUV data collected at 25 kHz underline the complexity of the situation. For a given NUV laser pulse energy, the data collected at 25 kHz pulse frequency generally show (1) lower measured oxygen concentrations and (2) lower O^+ IFs compared to 250 kHz pulsing. This implies that while field is the primary determinant factor, there may also be a kinetic component that requires further exploration. It also brings up an interesting question: what would the EUV data look like

if we could pulse at 250 kHz? Would we see a similar increase in the measured oxygen concentration? How might that change the calibration curve of oxygen concentration as a function of Mg^{++} CSF in Figure 6?

Another interesting point to consider is whether the same results would be obtained for different crystallographic orientations of MgO. The work functions of the {100}, {110} and {111} surfaces vary by up to 17 % [85] and even more interesting, the {111} surface is polar [86]. Bulk terminations have an infinite macroscopic dipole moment due to the presence of uncompensated Mg^{++} or O^{--} charge on individual layers. A consequence is that polar surfaces in ionic materials, including MgO, must always be charge compensated, e.g. reconstructed [87]. Given that the local bonding neighborhood and coordination at the surface selvedge would differ from that of the bulk, this may affect field evaporation in an interesting way that could be studied using NUV and EUV pulsing.

Finally, the existence of an apparent “universal” oxygen concentration calibration curve for both NUV and EUV laser pulsing is interesting. For subgap radiation, it may support the ideas that absorption in this material can occur through the closing of the bulk bandgap, photo-excited holes accumulating at the specimen apex, and/or corner or edge site atoms having a significantly reduced band gap [46,57,58,60,88,89]. Once a photon is absorbed, however, it appears the subsequent field evaporation (or ionization and desorption) occur via a similar pathway regardless of the incident laser wavelength. There are small differences in the mass spectra between the NUV and EUV experiments, but the overall trends are remarkably similar considering the > 10 X difference in photon energy. For example, the mass spectra for 0.005 % T and 0.01 pJ at 10 % DR, having nearly identical CSFs and oxygen concentrations, are nearly indistinguishable from each other. It may be that for materials like MgO that have a sub-gap absorption pathway, photon energies above the optical bandgap may confer no additional benefit.

Crystalline MgO is a strongly ionic compound with well-defined charged edge and corner sites. This may explain the differences with our previous experimental observations on amorphous SiO_2 and Al_2O_3 [26,39,90]. Indeed, a study comparing energy deficits in MgO and SiO_2 showed that these two materials behave very differently in pulsed laser APT [91].

Declarations of interest: none.

Acknowledgements

The authors thank Norman A. Sanford for assisting with sample preparation.

Author Contribution Statement

ANC Conceptualization, Formal analysis, Funding acquisition, Investigation, Project administration, Supervision, Visualization, Writing-original draft.

BWC Formal analysis, Investigation, Writing-review and editing.

CEM Investigation, Writing-review and editing.

JMG Investigation, Writing-review and editing.

LMA Investigation, Writing-review and editing.

References

[1] L. Mancini, N. Amirifar, D. Shinde, I. Blum, M. Gilbert, A. Vella, F. Vurpillot, W. Lefebvre, R. Lardé, E. Talbot, P. Pareige, X. Portier, A. Ziani, C. Davesnne, C. Durand, J. Eymery, R. Butté, J.F. Carlin, N. Grandjean, L. Rigutti, Composition of wide bandgap semiconductor materials and nanostructures measured by atom probe tomography and its dependence on the surface electric field, Journal of Physical Chemistry C 118 (2014) 24136–24151. https://doi.org/10.1021/JP5071264.

[2] E. Di Russo, I. Blum, J. Houard, M. Gilbert, G. Da Costa, D. Blavette, L. Rigutti, Compositional accuracy of atom probe tomography measurements in GaN: Impact of experimental parameters and multiple evaporation events, Ultramicroscopy 187 (2018) 126–134. https://doi.org/10.1016/J.ULTRAMIC.2018.02.001.

[3] D.R. Diercks, B.P. Gorman, Nanoscale Measurement of Laser-Induced Temperature Rise and Field Evaporation Effects in CdTe and GaN, Journal of Physical Chemistry C 119 (2015) 20623–20631. https://doi.org/10.1021/ACS.JPCC.5B02126/ASSET/IMAGES/LARGE/JP-2015-021269_0009.JPEG.

[4] L. Rigutti, L. Mancini, D. Hernández-Maldonado, W. Lefebvre, E. Giraud, R. Butté, J.F. Carlin, N. Grandjean, D. Blavette, F. Vurpillot, Statistical correction of atom probe tomography data of semiconductor alloys combined with optical spectroscopy: The case of Al0.25Ga0.75N, J. Appl. Phys. 119 (2016) 105704. https://doi.org/10.1063/1.4943612/140999.

[5] R.J.H. Morris, R. Cuduvally, J.R. Lin, M. Zhao, W. Vandervorst, M. Thuvander, C. Fleischmann, Field dependent study on the impact of co-evaporated multihits and ion pile-up for the apparent stoichiometric quantification of GaN and AlN, Ultramicroscopy 241 (2022) 113592. https://doi.org/10.1016/J.ULTRAMIC.2022.113592.

[6] Richard.J.H. Morris, R. Cuduvally, D. Melkonyan, C. Fleischmann, M. Zhao, L. Arnoldi, P. van der Heide, W. Vandervorst, Toward accurate composition analysis of GaN and AlGaN using atom probe tomography, Journal of Vacuum Science & Technology B, Nanotechnology and Microelectronics: Materials, Processing, Measurement, and Phenomena 36 (2018) 3–130. https://doi.org/10.1116/1.5019693/591796.

[7] L. Miaja-Avila, B.W. Caplins, A.N. Chiaramonti, P.T. Blanchard, M.D. Brubaker, A. V. Davydov, D.R. Diercks, B.P. Gorman, A. Rishinaramangalam, D.F. Feezell, K.A. Bertness, N.A. Sanford, Extreme Ultraviolet Radiation Pulsed Atom Probe Tomography of III-Nitride Semiconductor Materials, Journal of Physical Chemistry C 125 (2021) 2626–2635. https://doi.org/10.1021/ACS.JPCC.0C08753/ASSET/IMAGES/LARGE/JP0C08753_0007.JPEG.

[8] R.J.H. Morris, J.R. Lin, J.E. Scheerder, M.I. Popovici, J. Meersschaut, L. Goux, G.S. Kar, P. Van Der Heide, C. Fleischmann, Significant Oxygen Underestimation When Quantifying Barium-Doped SrTiO Layers by Atom Probe Tomography, Microscopy and Microanalysis 30 (2024) 49–58. https://doi.org/10.1093/MICMIC/OZAD144.

[9] J.R. Riley, R.A. Bernal, Q. Li, H.D. Espinosa, G.T. Wang, L.J. Lauhon, Atom probe tomography of a-axis GaN nanowires: Analysis of nonstoichiometric evaporation behavior, ACS Nano 6 (2012) 3898–3906. https://doi.org/10.1021/NN2050517.

[10] D.R. Diercks, B.P. Gorman, R. Kirchhofer, N. Sanford, K. Bertness, M. Brubaker, Atom probe tomography evaporation behavior of C-axis GaN nanowires: Crystallographic, stoichiometric, and detection efficiency aspects, J. Appl. Phys. 114 (2013) 184903. https://doi.org/10.1063/1.4830023/139812.

[11] D. Zanuttini, I. Blum, L. Rigutti, F. Vurpillot, J. Douady, E. Jacquet, P.M. Anglade, B. Gervais, Simulation of field-induced molecular dissociation in atom-probe tomography: Identification of a neutral emission channel, Phys. Rev. A (Coll. Park). 95 (2017) 061401. https://doi.org/10.1103/PHYSREVA.95.061401/DELIVERABLE/5ECC0302-75A4-4848-AE28-A9B9C8A5E1B6.

[12] R. Agrawal, R.A. Bernal, D. Isheim, H.D. Espinosa, Characterizing atomic composition and dopant distribution in wide band gap semiconductor nanowires using laser-assisted atom probe tomography, Journal of Physical Chemistry C 115 (2011) 17688–17694. https://doi.org/10.1021/JP2047823.

[13] N. Dawahre, G. Shen, S.N. Renfrow, S.M. Kim, P. Kung, Atom probe tomography of AlInN/GaN HEMT structures, Journal of Vacuum Science & Technology B, Nanotechnology and Microelectronics: Materials, Processing, Measurement, and Phenomena 31 (2013) 41802. https://doi.org/10.1116/1.4807321/467285.

[14] M. Hans, J.M. Schneider, On the chemical composition of TiAlN thin films - Comparison of ion beam analysis and laser-assisted atom probe tomography with varying laser pulse energy, Thin Solid Films 688 (2019) 137251. https://doi.org/10.1016/J.TSF.2019.04.026.

[15] E. Di Russo, N. Cherkashin, M. Korytov, A.E. Nikolaev, A. V. Sakharov, A.F. Tsatsulnikov, B. Bonef, I. Blum, J. Houard, G. Da Costa, D. Blavette, L. Rigutti, Compositional accuracy in atom probe tomography analyses performed on III-N light emitting diodes, J. Appl. Phys. 126 (2019) 124307. https://doi.org/10.1063/1.5113799/1063301.

[16] E. Di Russo, F. Moyon, N. Gogneau, L. Largeau, E. Giraud, J.F. Carlin, N. Grandjean, J.M. Chauveau, M. Hugues, I. Blum, W. Lefebvre, F. Vurpillot, D. Blavette, L. Rigutti, Composition Metrology of Ternary Semiconductor Alloys Analyzed by Atom Probe Tomography, Journal of Physical Chemistry C 122 (2018) 16704–16714. https://doi.org/10.1021/ACS.JPCC.8B03223/ASSET/IMAGES/LARGE/JP-2018-03223D_0007.JPEG.

[17] J.R. Riley, T. Detchprohm, C. Wetzel, L.J. Lauhon, On the reliable analysis of indium mole fraction within In xGa1-xN quantum wells using atom probe tomography, Appl. Phys. Lett. 104 (2014) 152102. https://doi.org/10.1063/1.4871510/131005.

[18] S.H. Kim, S. Bhatt, D.K. Schreiber, J. Neugebauer, C. Freysoldt, B. Gault, S. Katnagallu, Understanding atom probe's analytical performance for iron oxides using correlation histograms and ab initio calculations, New J. Phys. 26 (2024) 033021. https://doi.org/10.1088/1367-2630/AD309E.

[19] D. Schreiber, K. Kruska, K. Yano, A. Chiaramonti, Considerations for using Calibration Curves to Infer Oxide Stoichiometry from Atom Probe Tomography Data, Microscopy and Microanalysis 30 (2024) 40–41. https://doi.org/10.1093/MAM/OZAE044.018.

[20] D.K. Schreiber, A.N. Chiaramonti, K. Kruska, Compositional Dependencies of Ni- and Fe-oxides to Experimental Parameters in Atom Probe Tomography, in: 2020 TMS Annual Meeting & Exhibition, 2020.

[21] D.K. Schreiber, A.N. Chiaramonti, L.M. Gordon, K. Kruska, Applicability of post-ionization theory to laser-assisted field evaporation of magnetite, Appl. Phys. Lett. 105 (2014). https://doi.org/10.1063/1.4904802.

[22] M. Bachhav, F. Danoix, B. Hannoyer, J.M. Bassat, R. Danoix, Investigation of O-18 enriched hematite (α-Fe2O3) by laser assisted atom probe tomography, Int. J. Mass Spectrom. 335 (2013) 57–60. https://doi.org/10.1016/J.IJMS.2012.10.012.

[23] C. Cappelli, A. Prez-Huerta, Testing the Influence of Laser Pulse Energy and Rate in the Atom Probe Tomography Analysis of Minerals, Microscopy and Microanalysis 29 (2023) 1137–1152. https://doi.org/10.1093/MICMIC/OZAD057.

[24] C. Oberdorfer, P. Stender, C. Reinke, G. Schmitz, Laser-Assisted Atom Probe Tomography of Oxide Materials, Microscopy and Microanalysis 13 (2007) 342–346. https://doi.org/10.1017/S1431927607070274.

[25] N. Amirifar, R. Lardé, E. Talbot, P. Pareige, L. Rigutti, L. Mancini, J. Houard, C. Castro, V. Sallet, E. Zehani, S. Hassani, C. Sartel, A. Ziani, X. Portier, Quantitative analysis of doped/undoped ZnO nanomaterials using laser assisted atom probe tomography: Influence of the analysis parameters, J. Appl. Phys. 118 (2015) 215703. https://doi.org/10.1063/1.4936167/140328.

[26] A.N. Chiaramonti, L. Miaja-Avila, B.W. Caplins, P.T. Blanchard, D.R. DIercks, B.P. Gorman, N.A. Sanford, Field Ion Emission in an Atom Probe Microscope Triggered by Femtosecond-Pulsed Coherent Extreme Ultraviolet Light, Microscopy and Microanalysis 26 (2020) 258–266. https://doi.org/10.1017/S1431927620000203.

[27] E.A. Marquis, N.A. Yahya, D.J. Larson, M.K. Miller, R.I. Todd, Probing the improbable: imaging C atoms in alumina, Materials Today 13 (2010) 34–36. https://doi.org/10.1016/S1369-7021(10)70184-X.

[28] T. Kinno, M. Tomita, T. Ohkubo, S. Takeno, K. Hono, Laser-assisted atom probe tomography of 18O-enriched oxide thin film for quantitative analysis of oxygen, Appl. Surf. Sci. 290 (2014) 194–198. https://doi.org/10.1016/J.APSUSC.2013.11.039.

[29] Y.M. Chen, T. Ohkubo, M. Kodzuka, K. Morita, K. Hono, Laser-assisted atom probe analysis of zirconia/spinel nanocomposite ceramics, Scr. Mater. 61 (2009) 693–696. https://doi.org/10.1016/j.scriptamat.2009.05.043.

[30] M. Karahka, Y. Xia, H.J. Kreuzer, The mystery of missing species in atom probe tomography of composite materials, Appl. Phys. Lett. 107 (2015) 62105. https://doi.org/10.1063/1.4928625/29302.

[31] D. Larson, R. Alvis, D. Lawrence, T. Prosa, R. Ulfig, D. Reinhard, P. Clifton, S. Gerstl, J. Bunton, D. Lenz, T. Kelly, K. Stiller, Analysis of Bulk Dielectrics with Atom Probe Tomography, Microscopy and Microanalysis 14 (2008) 1254–1255. https://doi.org/10.1017/S1431927608083657.

[32] C. Cappelli, S. Smart, H. Stowell, A. Pérez-Huerta, Exploring Biases in Atom Probe Tomography Compositional Analysis of Minerals, Geostand. Geoanal. Res. 45 (2021) 457–476. https://doi.org/10.1111/GGR.12395/ABSTRACT.

[33] D.A. Reinhard, D.E. Moser, I. Martin, K.P. Rice, Y. Chen, D. Olson, D. Lawrence, T.J. Prosa, D.J. Larson, Atom Probe Tomography of Phalaborwa Baddeleyite and Reference Zircon BR266, Microstructural Geochronology: Planetary Records Down to Atom Scale (2017) 315–326. https://doi.org/10.1002/9781119227250.CH15.

[34] C. Cappelli, A. Pérez-Huerta, Effect of crystallographic orientation on atom probe tomography geochemical data?, Micron 137 (2020). https://doi.org/10.1016/J.MICRON.2020.102910.

[35] K.A. Hunnestad, C. Hatzoglou, F. Vurpillot, I.E. Nylund, Z. Yan, E. Bourret, A.T.J. van Helvoort, D. Meier, Correlating laser energy with compositional and atomic-level information of oxides in atom probe tomography, Mater. Charact. 203 (2023) 113085. https://doi.org/10.1016/J.MATCHAR.2023.113085.

[36] F. Exertier, A. La Fontaine, C. Corcoran, S. Piazolo, E. Belousova, Z. Peng, B. Gault, D.W. Saxey, D. Fougerouse, S.M. Reddy, S. Pedrazzini, P.A.J. Bagot, M.P. Moody, B. Langelier, D.E. Moser, G.A. Botton, F. Vogel, G.B. Thompson, P.T. Blanchard, A.N. Chiaramonti, D.A. Reinhard, K.P. Rice, D.K. Schreiber, K. Kruska, J. Wang, J.M. Cairney, Atom probe tomography analysis of the reference zircon gj-1: An interlaboratory study, Chem. Geol. 495 (2018). https://doi.org/10.1016/j.chemgeo.2018.07.031.

[37] A. Cerezo, A.K. Petford-Long, D.J. Larson, S. Pinitsoontorn, E.W. Singleton, The formation mechanism of aluminium oxide tunnel barriers, Journal of Materials Science 2006 41:23 41 (2006) 7843–7852. https://doi.org/10.1007/S10853-006-0562-1.

[38] D. Zanuttini, I. Blum, L. Rigutti, F. Vurpillot, J. Douady, E. Jacquet, P.M. Anglade, B. Gervais, Simulation of field-induced molecular dissociation in atom-probe tomography: Identification of a neutral emission channel, Phys. Rev. A (Coll. Park). 95 (2017). https://doi.org/10.1103/PHYSREVA.95.061401.

[39] J.M. Garcia, A.N. Chiaramonti, B.W. Caplins, L. Miaja-Avila, N.A. Sanford, Comprehensive Experimental Study of Insulating Aluminum Oxide (α-Al2O3) Using NUV- and EUV-Pulsed Atom Probe Tomography, Microscopy and Microanalysis 30 (2024) 101–103. https://doi.org/10.1093/MAM/OZAE044.051.

[40] S. Gin, J.V. Ryan, D.K. Schreiber, J. Neeway, M. Cabié, Contribution of atom-probe tomography to a better understanding of glass alteration mechanisms: Application to a nuclear glass specimen altered 25 years in a granitic environment, Chem. Geol. 349–350 (2013) 99–109. https://doi.org/10.1016/J.CHEMGEO.2013.04.001.

[41] T. Veret, F. Delaroche, I. Blum, J. Houard, B. Klaes, I. Mouton, F. De-Geuser, A.-M. Seydoux-Guillaume, F. Vurpillot, Exploring mechanisms leading to composition errors in monazite (CePO4) analysed with atom probe tomography, (2025). https://arxiv.org/abs/2511.02617v1 (accessed March 8, 2026).

[42] B. Mazumder, X. Liu, R. Yeluri, F. Wu, U.K. Mishra, J.S. Speck, Atom probe tomography studies of Al2O3 gate dielectrics on GaN, J. Appl. Phys. 116 (2014) 134101. https://doi.org/10.1063/1.4896498/857318.

[43] D. Santhanagopalan, D.K. Schreiber, D.E. Perea, R.L. Martens, Y. Janssen, P. Khalifah, Y.S. Meng, Effects of laser energy and wavelength on the analysis of LiFePO4 using laser assisted atom probe tomography, Ultramicroscopy 148 (2015) 57–66. https://doi.org/10.1016/J.ULTRAMIC.2014.09.004.

[44] F. Chabanais, E. Di Russo, A. Karg, M. Eickhoff, W. Lefebvre, L. Rigutti, Behavior of the ε-Ga2O3:Sn Evaporation During Laser-Assisted Atom Probe Tomography, Microscopy and Microanalysis 27 (2021) 687–695. https://doi.org/10.1017/S1431927621000544.

[45] M. Krämer, B. Favelukis, J.M. Prabhakar, A. Albrecht, B.A. Rosen, N. Eliaz, M. Sokol, B. Gault, Compositional complexity in a 2D transition metal oxide, Mater. Today Nano 34 (2026) 100790. https://doi.org/10.1016/J.MTNANO.2026.100790.

[46] Y.M. Chen, T. Ohkubo, K. Hono, Laser assisted field evaporation of oxides in atom probe analysis, Ultramicroscopy 111 (2011) 562–566. https://doi.org/10.1016/j.ultramic.2010.12.013.

[47] B. Mazumder, A. Vella, B. Deconihout, T. Al-Kassab, Evaporation mechanisms of MgO in laser assisted atom probe tomography, Ultramicroscopy 111 (2011) 571–575. https://doi.org/10.1016/j.ultramic.2010.11.017.

[48] A. Vella, B. Mazumder, G. Da Costa, B. Deconihout, Field evaporation mechanism of bulk oxides under ultra fast laser illumination, J. Appl. Phys. 110 (2011) 044321. https://doi.org/10.1063/1.3610523.

[49] A. Devaraj, R. Colby, F. Vurpillot, S. Thevuthasan, Understanding Atom Probe Tomography of Oxide-Supported Metal Nanoparticles by Correlation with Atomic-Resolution Electron Microscopy and Field Evaporation Simulation, J. Phys. Chem. Lett. 5 (2014) 1361–1367. https://doi.org/10.1021/jz500259c.

[50] K. Stiller, L. Viskari, G. Sundell, F. Liu, M. Thuvander, H.-O. Andrén, D.J. Larson, T. Prosa, D. Reinhard, Atom Probe Tomography of Oxide Scales, Oxidation of Metals 79 (2013) 227–238. https://doi.org/10.1007/s11085-012-9330-6.

[51] J.B. Seol, C.M. Kwak, Y.T. Kim, C.G. Park, Understanding of the field evaporation of surface modified oxide materials through transmission electron microscopy and atom probe tomography, Appl. Surf. Sci. 368 (2016) 368–377. https://doi.org/10.1016/J.APSUSC.2016.01.196.

[52] E.A. MARQUIS, B.P. GEISER, T.J. PROSA, D.J. LARSON, Evolution of tip shape during field evaporation of complex multilayer structures, J. Microsc. 241 (2011) 225–233. https://doi.org/10.1111/j.1365-2818.2010.03421.x.

[53] A.G. Joly, M. Henyk, K.M. Beck, P.E. Trevisanutto, P. V. Sushko, W.P. Hess, A.L. Shluger, Probing electron transfer dynamics at MgO surfaces by Mg-atom desorption, Journal of Physical Chemistry B 110 (2006) 18093–18096. https://doi.org/10.1021/JP064092B/ASSET/IMAGES/MEDIUM/JP064092BE00002.GIF.

[54] K.M. Beck, A.G. Joly, O. Diwald, S. Stankic, P.E. Trevisanutto, P. V. Sushko, A.L. Shluger, W.P. Hess, Energy and site selectivity in O-atom photodesorption from nanostructured MgO, Surf. Sci. 602 (2008) 1968–1973. https://doi.org/10.1016/J.SUSC.2008.03.046.

[55] K.M. Beck, A.G. Joly, W.P. Hess, Effect of Surface Charge on Laser-induced Neutral Atom Desorption, Applied Physics A, Materials Science and Processing, 101(1):61-64 101 (2010) 61–64. https://doi.org/10.1007/S00339-010-5758-1.

[56] W.P. Hess, A.G. Joly, K.M. Beck, R.M. Williams, J.T. Dickinson, Femtosecond time-resolved laser-induced desorption of positive ions from MgO, Appl. Phys. A Mater. Sci. Process. 69 (1999) S389–S393. https://doi.org/10.1007/S003390051423/METRICS.

[57] M. Tsukada, H. Tamura, K.P. McKenna, A.L. Shluger, Y.M. Chen, T. Ohkubo, K. Hono, Mechanism of laser assisted field evaporation from insulating oxides, Ultramicroscopy 111 (2011) 567–570. https://doi.org/10.1016/j.ultramic.2010.11.011.

[58] H. Tamura, M. Tsukada, K.P. McKenna, A.L. Shluger, T. Ohkubo, K. Hono, Laser-assisted field evaporation from insulators triggered by photoinduced hole accumulation, Phys. Rev. B Condens. Matter Mater. Phys. 86 (2012) 195430. https://doi.org/10.1103/PhysRevB.86.195430.

[59] Y. Xia, L. Tang, X. Lu, S. Zhu, Theoretical insights into laser-assisted field evaporation of ionic compounds, J. Appl. Phys. 136 (2024) 134304. https://doi.org/10.1063/5.0231078/3315096.

[60] E.P. Silaeva, M. Karahka, H.J. Kreuzer, Atom Probe Tomography and field evaporation of insulators and semiconductors: Theoretical issues, Curr. Opin. Solid State Mater. Sci. 17 (2013) 211–216. https://doi.org/10.1016/J.COSSMS.2013.08.001.

[61] M. Karahka, H.J. Kreuzer, Field evaporation of oxides: a theoretical study, Ultramicroscopy 132 (2013) 54–59. https://doi.org/10.1016/J.ULTRAMIC.2012.10.007.

[62] Y. Xia, Z. Li, Laser-assisted field evaporation of metal oxides: A time-dependent density functional theory study, Journal of Chemical Physics 145 (2016) 204704. https://doi.org/10.1063/1.4968213/281260.

[63] K. Thompson, D. Lawrence, D.J. Larson, J.D. Olson, T.F. Kelly, B. Gorman, In situ site-specific specimen preparation for atom probe tomography, Ultramicroscopy 107 (2007) 131–139. https://doi.org/10.1016/J.ULTRAMIC.2006.06.008.

[64] B.W. Caplins, A.N. Chiaramonti, J.M. Garcia, N.A. Sanford, L. Miaja-Avila, Atom probe tomography using an extreme ultraviolet trigger pulse Articles You May Be Interested In The Trigger Algorithm for the Burst Alert Telescope on Swift Spark-Gap Trigger System Atom probe tomography using an extreme ultraviolet trigger pulse, Cite as: Rev. Sci. Instrum 94 (2023) 93704. https://doi.org/10.1063/5.0160797.

[65] A.N. Chiaramonti, L. Miaja-Avila, P.T. Blanchard, D.R. Diercks, B.P. Gorman, N.A. Sanford, A Three-Dimensional Atom Probe Microscope Incorporating a Wavelength-Tuneable Femtosecond-Pulsed Coherent Extreme Ultraviolet Light Source, MRS Adv. 4 (2019) 2367–2375. https://doi.org/10.1557/adv.2019.296.

[66] L. Tegg, L.T. Stephenson, J.M. Cairney, Estimation of the Electric Field in Atom Probe Tomography Experiments Using Charge State Ratios, Microscopy and Microanalysis 30 (2024) 466–475. https://doi.org/10.1093/MAM/OZAE047.

[67] R.J.H. Morris, R. Cuduvally, D. Melkonyan, M. Zhao, P. van der Heide, W. Vandervorst, Atom probe of GaN/AlGaN heterostructures: The role of electric field, sample crystallography and laser excitation on quantification, Ultramicroscopy 206 (2019). https://doi.org/10.1016/j.ultramic.2019.112813.

[68] E. Di Russo, F. Vurpillot, L. Rigutti, Compositional Metrology of Atom Probe Applied to non-Metallic Materials , ArXiv (2026). https://doi.org/https://doi.org/10.48550/arXiv.2602.14565.

[69] D.R. Kingham, The post-ionization of field evaporated ions: A theoretical explanation of multiple charge states, Surf. Sci. 116 (1982) 273–301. https://doi.org/10.1016/0039-6028(82)90434-4.

[70] A. Rundquist, C.G. Durfee, Z. Chang, C. Herne, S. Backus, M.M. Murnane, H.C. Kapteyn, Phase-matched generation of coherent soft X-rays, Science 280 (1998) 1412–5. https://doi.org/10.1126/science.280.5368.1412.

[71] B.N. Taylor, Guidelines for evaluating and expressing the uncertainty of NIST measurement results, (1994). https://doi.org/10.6028/NIST.TN.1297.

[72] International Organization for Standardization, ISO 98-1:2024 Guide to the expression of uncertainty in measurement, 2024. https://www.iso.org/obp/ui/en/#iso:std:iso-iec:guide:98:-1:ed-2:v1:en (accessed March 4, 2026).

[73] F. Meisenkothen, E.B. Steel, T.J. Prosa, K.T. Henry, R. Prakash Kolli, Effects of detector dead-time on quantitative analyses involving boron and multi-hit detection events in atom probe tomography, Ultramicroscopy 159 (2015). https://doi.org/10.1016/j.ultramic.2015.07.009.

[74] F. Meisenkothen, D. V. Samarov, I. Kalish, E.B. Steel, Exploring the accuracy of isotopic analyses in atom probe mass spectrometry, Ultramicroscopy 216 (2020) 113018. https://doi.org/10.1016/J.ULTRAMIC.2020.113018.

[75] D.J. Larson, T.J. Prosa, R.M. Ulfig, B.P. Geiser, T.F. Kelly, Local Electrode Atom Probe Tomography, Springer New York, New York, NY, 2013. https://doi.org/10.1007/978-1-4614-8721-0.

[76] B.W. Caplins, P.T. Blanchard, A.N. Chiaramonti, D.R. Diercks, L. Miaja-Avila, N.A. Sanford, An algorithm for correcting systematic energy deficits in the atom probe mass spectra of insulating samples, Ultramicroscopy 213 (2020) 112995. https://doi.org/10.1016/j.ultramic.2020.112995.

[77] M.N. Bachhav, R. Danoix, F. Vurpillot, B. Hannoyer, S.B. Ogale, F. Danoix, Evidence of lateral heat transfer during laser assisted atom probe tomography analysis of large band gap materials, Appl. Phys. Lett. 99 (2011) 84101. https://doi.org/10.1063/1.3622647/123432.

[78] Z. Peng, D. Zanuttini, B. Gervais, E. Jacquet, I. Blum, P.P. Choi, D. Raabe, F. Vurpillot, B. Gault, Unraveling the Metastability of Cn2+ (n = 2-4) Clusters, Journal of Physical Chemistry Letters 10 (2019) 581–588. https://doi.org/10.1021/ACS.JPCLETT.8B03449/ASSET/IMAGES/LARGE/JZ-2018-03449E_0003.JPEG.

[79] B.W. Caplins, A.N. Chiaramonti, J.M. Garcia, L. Miaja-Avila, K.H. Yano, D.K. Schreiber, J.H. Bunton, On the instrument-dependent appearance of ion dissociation events in atom probe tomography mass spectra, Ultramicroscopy 267 (2024) 114061. https://doi.org/10.1016/J.ULTRAMIC.2024.114061.

[80] I. Blum, L. Rigutti, F. Vurpillot, A. Vella, A. Gaillard, B. Deconihout, Dissociation Dynamics of Molecular Ions in High dc Electric Field, Journal of Physical Chemistry A 120 (2016) 3654–3662. https://doi.org/10.1021/ACS.JPCA.6B01791.

[81] I. Blum, D. Zanuttini, L. Rigutti, F. Vurpillot, J. Douady, E. Jacquet, P.-M. Anglade, B. Gervais, A. Vella, A. Gaillard, Dissociation of Molecular Ions During the DC Field Evaporation ZnO in Atom Probe Tomography, Microscopy and Microanalysis 22 (2016) 662–663. https://doi.org/10.1017/S1431927616004165.

[82] T. Veret, F. Delaroche, I. Blum, J. Houard, B. Klaes, I. Mouton, F. De-Geuser, A.M. Seydoux-Guillaume, F. Vurpillot, Exploring Mechanisms Leading to Composition Errors in Monazite (CePO4) Analyzed With Atom Probe Tomography, Microscopy and Microanalysis 32 (2026) 9. https://doi.org/10.1093/MAM/OZAG009.

[83] D.W. Saxey, Correlated ion analysis and the interpretation of atom probe mass spectra, Ultramicroscopy 111 (2011) 473–479. https://doi.org/10.1016/j.ultramic.2010.11.021.

[84] Y. Xia, Z. Li, Laser-assisted field evaporation of metal oxides: A time-dependent density functional theory study, Journal of Chemical Physics 145 (2016). https://doi.org/10.1063/1.4968213/281260.

[85] E.H. Choi, J.Y. Lim, S.O. Kang, H.S. Uhm, Measurement of work function at MgO crystal surface by the γ-focused ion beam system, Japanese Journal of Applied Physics, Part 2: Letters 41 (2002) L1006. https://doi.org/10.1143/JJAP.41.L1006/XML.

[86] C. Noguera, Polar oxide surfaces, Journal of Physics: Condensed Matter 12 (2000) R367. https://doi.org/10.1088/0953-8984/12/31/201.

[87] D. Wolf, Structure of ionic interfaces from an absolutely convergent solution of the Madelung problem, Solid State Ion. 75 (1995) 3–11. https://doi.org/10.1016/0167-2738(94)00183-S.

[88] M. Sterrer, O. Diwald, E. Knözinger, P. V. Sushko, A.L. Shluger, Energies and dynamics of photoinduced electron and hole processes on MgO powders, Journal of Physical Chemistry B 106 (2002) 12478–12482. https://doi.org/10.1021/JP026733I/ASSET/IMAGES/LARGE/JP026733IF00005.JPEG.

[89] S. Stankic, J. Bernardi, O. Diwald, E. Knözinger, Optical surface properties and morphology of MgO and CaO nanocrystals, J. Phys. Chem. B 110 (2006) 13866–13871. https://doi.org/10.1021/JP061741A.

[90] J.M. Garcia, B.W. Caplins, A.N. Chiaramonti, L. Miaja-Avila, N.A. Sanford, A Comprehensive Examination of Aluminum Oxide (Al2O3) Using Extreme and Near Ultraviolet Laser-Assisted Atom Probe Tomography, Microscopy and Microanalysis 29 (2023) 83–84. https://doi.org/10.1093/MICMIC/OZAD067.033.

[91] L. Arnoldi, E.P. Silaeva, A. Gaillard, F. Vurpillot, I. Blum, L. Rigutti, B. Deconihout, A. Vella, Energy deficit of pulsed-laser field-ionized and field-emitted ions from non-metallic nano-tips, J. Appl. Phys 115 (2014) 203705. https://doi.org/10.1063/1.4879315.

Supplementary Material

Mass spectral data is available at https://data.nist.gov/od/id/mds2-4005.

Supplementary Table 1: Measured Ga+ concentration and percent multiple hits for each of the experiments in this study.

	Laser Pulse Energy	Pulse Frequency	Detection Rate	Ga Concentration	Multiple Hits
	(p J)	(kHz)	(%)	(at. %)	(%)
NUV	100	25	1	not detected	27
	100	250	1	0.08	33
	100	250	10	0.05	40
	10	25	1	0.01	34
	10	250	1	0.01	34
	10	250	10	0.01	44
	1	25	1	0.02	37
	1	250	1	0.01	38
	1	250	10	not detected	54
	0.1	25	1	not detected	39
	0.1	250	1	0.01	48
	0.1	250	10	0.01	64
	0.01	25	1	0.04	51
	0.01	250	1	0.03	60
	0.01	250	10	0.19	71
	Percent Transmission	**Pulse Frequency**	**Detection Rate**	**Ga Concentration**	**Multiple Hits**
	(%)	**(kHz)**	**(%)**	**(at. %)**	**(%)**
EUV	0.005	25	1	0.06	59
	0.005	25	10	0.01	73
	0.05	25	1	0.06	51
	0.05	25	10	0.06	73
	0.5	25	1	0.15	45
	0.5	25	10	not detected	66
	5	25	1	0.39	59
	5	25	10	0.01	73

Supplementary Table 2: Oxygen concentration calculated using two different local range assisted background subtraction methods (power law and constant) and also calculated using no background subtraction (only the global time-of-flight background was applied).

Oxygen Concentration Using Three Different Background Subtraction Methods						
	Pulse Energy	Detection Rate	Pulse Frequency	Power Law Background	Constant Background	No Background
	(pJ)	(%)	(kHz)	(at. %)	(at. %)	(at. %)
NUV	100	1	250	49	59	37
NUV	0.01	1	250	52	48	43
	Percent Transmission	Detection Rate	Pulse Frequency	Power Law Background	Constant Background	No Background
	(%)	(%)	(kHz)	(at. %)	(at. %)	(at. %)
EUV	5	1	25	38	44	35
EUV	0.005	1	25	50	53	43

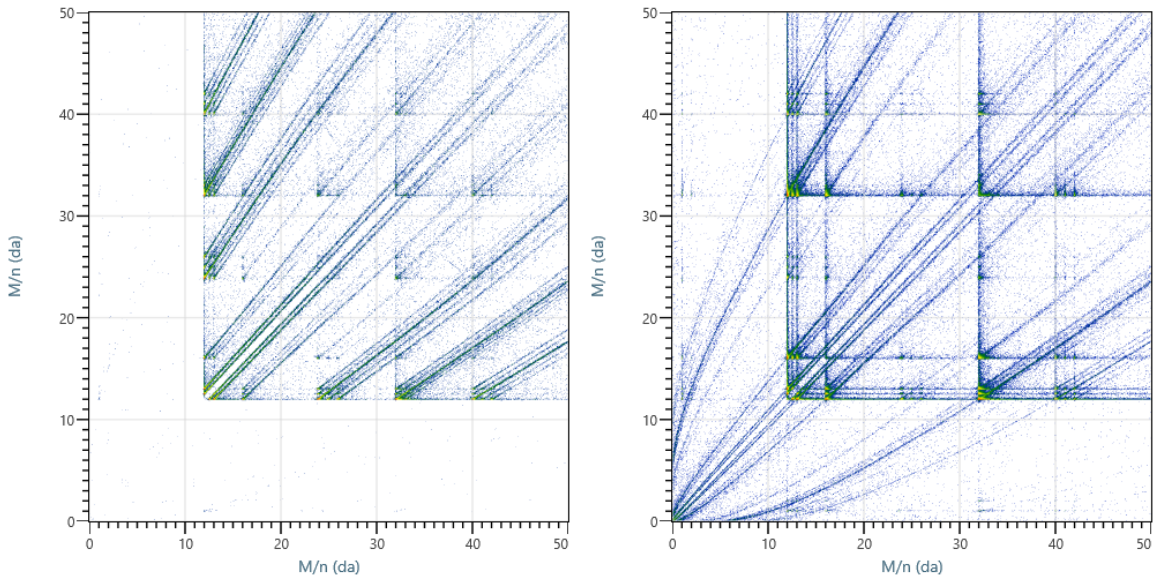

Supplementary Figure 1: Correlation histograms for NUV laser pulsing. (Left) 100 pJ, 250 kHz, 1 % DR. (Right) 0.01 pJ, 250 kHz, 1 % DR.

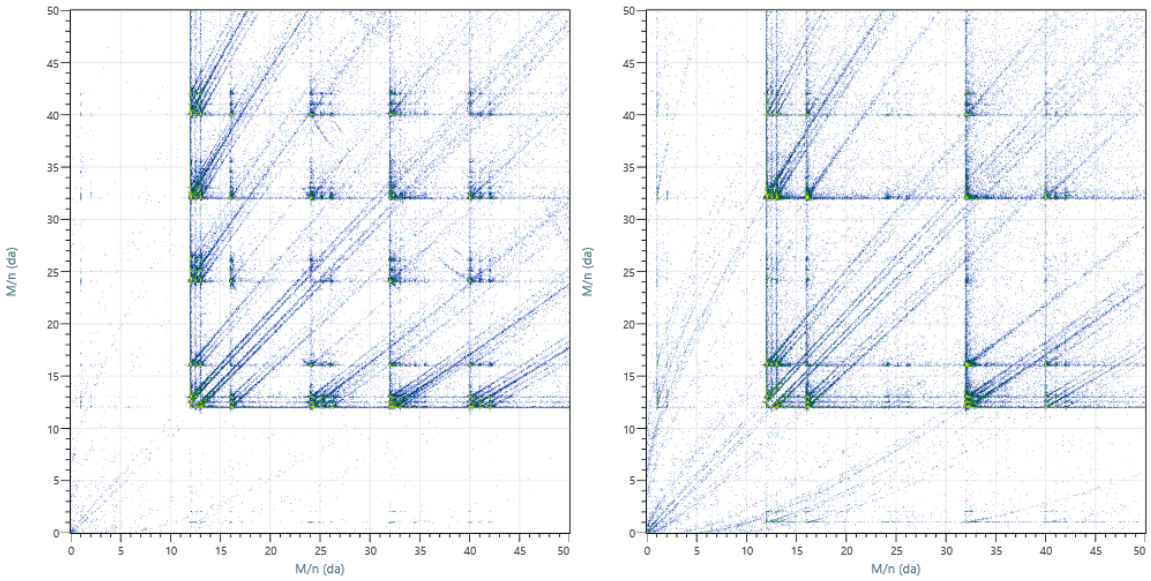

Supplementary Figure 2: Correlation histograms for EUV laser pulsing. (Left) 5 % T, 25 kHz, 1 % DR. (Right) 0.005 % T, 25 kHz, 1 % DR.

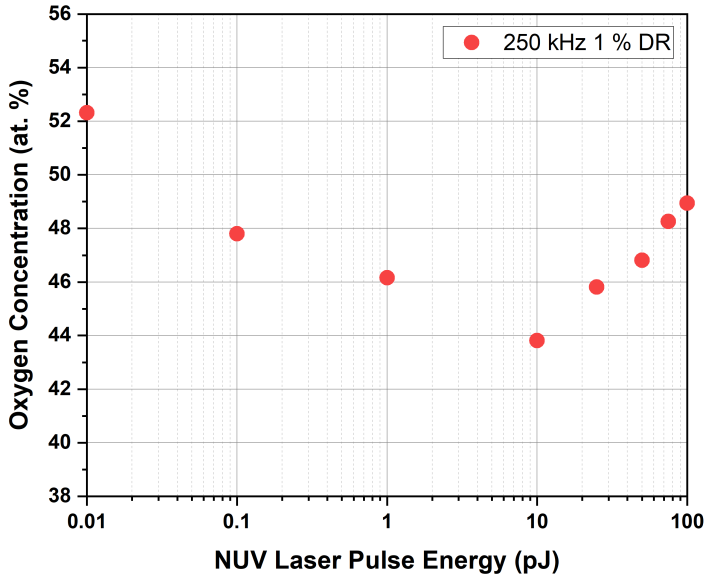

Supplementary Figure 3: NUV data collected at 250 kHz, 1 % DR showing additional points at 25 pJ, 50 pJ, and 75 pJ as further proof that the data collected at 100 pJ is real and forms a continuous curve.

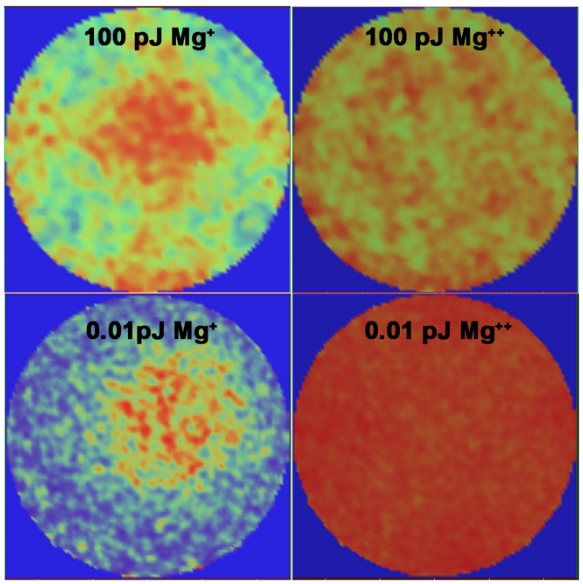

Supplementary Figure 4: Detector space maps showing spatial distribution of Mg+ and Mg++ ions for the highest and lowest NUV pulsing conditions. Each individual detector map measures 80 mm square.

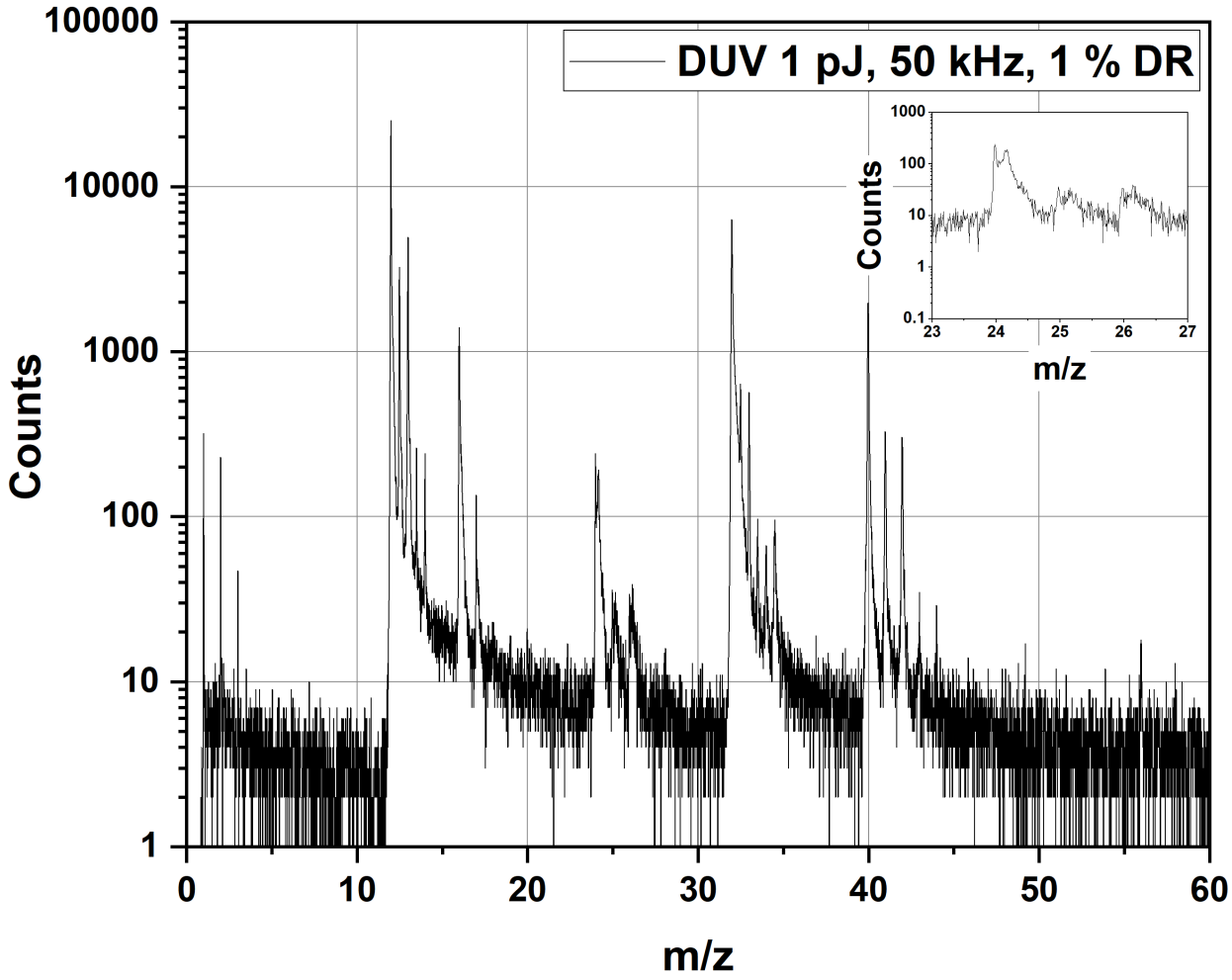

Supplementary Figure 5: Mass spectra binned to 0.01 m/z per bin from the same MgO single crystal as the study here. This data was collected on a commercial CAMECA Invizo 6000 straight flight path atom probe instrument equipped with a deep ultraviolet ((λ=257 nm; E_{photon}=4.8 eV) laser. Data was collected at 1 pJ, 50 kHz, and 1 % DR. The Mg^{++} peaks are split, as also observed in the NUV and EUV.